RESEARCH ARTICLE



Enhancing epidural needle guidance using a polarization-sensitive optical coherence tomography probe with convolutional neural networks

Chen Wang¹ | Yunlong Liu² | Paul Calle² | Xinwei Li³ | Ronghao Liu⁴ | Qinghao Zhang¹ | Feng Yan¹ | Kar-ming Fung^{5,6} | Andrew K. Conner⁷ | Sixia Chen⁸ | Chongle Pan² | Qinggong Tang¹

Correspondence

Chongle Pan, School of Computer Science, University of Oklahoma, Norman, OK 73019, USA. Email: cpan@ou.edu

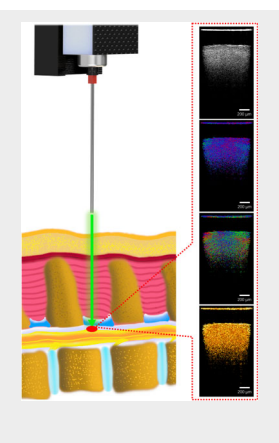
Qinggong Tang, Stephenson School of Biomedical Engineering, University of Oklahoma, Norman, OK 73019, USA. Email: qtang@ou.edu

Funding information

National Science Foundation, Grant/Award Numbers: OIA-2132161, 2238648; National Institutes of Health, Grant/Award Numbers: R01DK133717, P20GM135009, P20GM103639, P30CA225520, NIGMSU54GM104938; Oklahoma Center for the Advancement of Science and Technology, Grant/Award Number: HR23-071; OU Libraries' Open Access Fund: American Cancer Society. Grant/Award Number: IRG-19-142-01

Abstract

Epidural anesthesia helps manage pain during different surgeries. Nonetheless, the precise placement of the epidural needle remains a challenge. In this study, we developed a probe based on polarization-sensitive optical coherence tomography (PS-OCT) to enhance the epidural anesthesia needle placement. The probe was tested on six porcine spinal samples. The multimodal imaging guidance used the OCT intensity mode and three distinct PS-OCT modes: (1) phase retardation, (2) optic axis, and (3) degree of polarization uni-



formity (DOPU). Each mode enabled the classification of different epidural tissues through distinct imaging characteristics. To further streamline the tissue recognition procedure, convolutional neural network (CNN) were used to autonomously identify the tissue types within the probe's field of view. ResNet50 models were developed for all four imaging modes. DOPU imaging was found to provide the highest cross-testing accuracy of 91.53%. These results showed the improved precision by PS-OCT in guiding epidural anesthesia needle placement.

Chen Wang and Yunlong Liu contributed equally to this study.

¹Stephenson School of Biomedical Engineering, University of Oklahoma, Norman, Oklahoma, USA

²School of Computer Science, University of Oklahoma, Norman, Oklahoma, USA

³Department of Electrical and Electronic Engineering, University of Nottingham, Nottingham, UK

⁴School of Computer Science and Technology, Shandong Jianzhu University, Jinan, China

⁵Department of Pathology, University of Oklahoma Health Sciences Center, Oklahoma City, Oklahoma, USA

⁶Stephenson Cancer Center, University of Oklahoma Health Sciences Center, Oklahoma City, Oklahoma, USA

⁷Department of Neurosurgery, University of Oklahoma College of Medicine, Oklahoma City, Oklahoma, USA

⁸Department of Biostatistics and Epidemiology, Hudson College of Public Health, University of Oklahoma Health Sciences Center, Oklahoma City, Oklahoma, USA

KEYWORDS

deep-learning, endoscope, epidural anesthesia guidance, polarization-sensitive optical coherence tomography

1 | INTRODUCTION

Epidural anesthesia is a versatile and transformative anesthetic technique, which has improved pain relief and heightened patient satisfaction. The procedure finds application across the cervical, thoracic, and lumbar positions for a variety of operations, including cardiovascular surgery [1], stomach surgery [2], and painless delivery [3]. It helps relieve perioperative stress responses and symptoms. Epidural anesthesia involves the insertion of a needle into the epidural space, followed by the injection of local anesthetic around the spine. This procedure effectively blocks the transmission of pain signals from the spinal nerves to the brain. The epidural needle insertion generally aims to the vertebral spinous spaces or paramedian vertebral interspace [4]. During the insertion, the needle passes through subcutaneous fat, ligaments, and ligamentum flavum and then arrives at the epidural space where the spinal cord is located. Ensuring the precise placement of the epidural needle is critically important to achieve both efficacy and safety in the administration of epidural anesthesia. Any error in needle placement can lead to consequential complications. Postdural puncture headache (PDPH) is a frequently observed iatrogenic complication arising from inadvertent injury to the dura mater, with the overall incidence rate from 6% to 36% [5]. Epidural anesthesia is widely used in delivery when the estrogen secretion of the pregnant dramatically increases. Elevated estrogen levels can impact the tone of cerebral vessels, potentially leading to an increased vascular distension response to cerebrospinal fluid hypotension. As a consequence, pregnant mothers are at a heightened risk for PDPH [6]. Additionally, if the epidural needle is misplaced, it may lead to the occurrence of epidural hematomas, spinal cord damage, and abscess [7].

To sense the position of the epidural needle tip during its insertion, anesthesiologists generally employ a loss-of-resistance (LOR) technique. This involves continuously injecting saline or air into the needle via a syringe and monitoring the resulting feedback force. By doing so, they can sense the occurrence of the LOR, which indicates the successful traversal of various spinal tissues and the arrival of the needle to the epidural space [8]. However, LOR remains challenging in clinical practice as it lacks visual feedback. Needle insertion guided solely by LOR can lead to the failure rate of up to 20% [9].

To improve the precision of needle guidance in the administration of epidural anesthesia, various imaging techniques have been utilized. Notably, ultrasound has become a widely employed imaging modality for needle guidance during epidural anesthesia [10]. Real-time ultrasound has been demonstrated to increase the epidural needle placement accuracy [11]. Fluoroscopy has been employed to guide the epidural needle placement, particularly in non-obstetrical situations [12]. It was shown to enhance the success rate of needle insertion in cases involving adhesion and stenosis [13]. However, the resolutions of ultrasound and fluoroscopy are usually at millimeter level. Thus, ultrasound and fluoroscopy encounter challenges when attempting to discern the epidural space, which exhibits a width spanning from 2 to 3 mm in the cervical region and from 5 to 6 mm in the lumbar region [14, 15]. Furthermore, acoustic window of ultrasound is limited by the complex back bones. Fluoroscopy lacks soft tissue contrast, making it difficult to distinguish different tissues [9]. More recently, novel techniques such as fiberoptic bundle or optical spectral analysis have been reported [16, 17], but the movement of surrounding fluids or tissues in front of the imaging sites is likely to impact their imaging results.

We demonstrated the use of optical coherence tomography (OCT) for accurate identification of the epidural needle position by taking the advantages of its micrometer-level resolution in tissue visualization [18]. In our previous studies, we designed a forward-view swept-source OCT (SS-OCT) endoscopic system to visualize the tissues in front of the epidural needle [9, 19, 20]. To help anesthesiologists interpret the real-time imaging during the operation, we developed deep-learning models to automate the identification of tissue types from the OCT images [19]. The overall classification accuracy for identifying the correct tissue out of five tissue types was only approximately 66% [19]. To improve the tissue recognition accuracy, a series of binary classification models were developed by assuming a fixed sequence of spinal tissues to be encountered during the needle insertion. The average accuracy of 96.65% was achieved by the binary model, whereas the tissue was assumed to always manifest in a specific sequence corresponding to the epidural anatomy. The situations can be complicated as tissue distribution is not always ideal, hindering the clinical translation of the binary model.

In this study, we developed a polarization-sensitive OCT (PS-OCT) probe to improve the tissue recognition accuracy for epidural needle placement. PS-OCT represents an advancement over traditional intensity OCT as it enables the acquisition of polarization-related features through birefringence and diattenuation optical signals [21]. Because tissues such as nerve fibers exhibit strong polarization contrast signals, these additional polarization features may enhance the accuracy of spinal tissue recognition. The PS-OCT used in this study was equipped with much higher axial resolution (\sim 5.5 µm in air) compared to the previous SS-OCT system (\sim 14.0 μ m in air). Here, we developed a PS-OCT endoscope specifically designed to be fit inside the clinically used epidural needle and tested it on porcine backbone samples. The performance of PS-OCT for distinguishing the porcine backbone tissues was benchmarked in this research.

2 | METHODS

2.1 | Experimental setup

The experimental setup of our PS-OCT probe is shown in Figure 1. It is a single-input device with a unique PS detector unit, enabling simultaneous acquisition of two orthogonal polarization states at full imaging speed. A linear polarized fiber laser operating at a center wavelength of 1300 nm with a bandwidth of 170 nm served as the light source. The laser light was initially directed through a polarization-maintaining (PM) circulator, ensuring its transmission in a specific direction to facilitate the routing

of laser signals among various components. Upon traversing the circulator, the light was collimated within the space and divided into a reference arm and a sample arm using a beam splitter. The light directed into the sample arm was illuminated to the tissue, whereas the light routed into the reference arm served as the reference beam. A quarter-wave plate (QWP) rotated by 22.5° orientation was put in the reference arm and exited with a 45° linear polarization after passing through the QWP twice. Another QWP rotated by 45° was put in the sample arm to obtain circularly polarized light, which made the system sensitive to all polarization effects from the sample and independent of the orientation of the sample in plane. PM fiber was employed to ensure polarization preservation across the entire system. The two lights, which were either backscattered or reflected from the sample arm and reflected within the reference arm, converged at the beam splitter before re-entering the collimator. Subsequently, the resulting interference light was transmitted to the optical subsystem for postprocessing. The optical subsystem splits the interference light into the vertical linearly polarized signal and horizontal linearly polarized signal by two PS beam splitters, which are further detected and processed by two PS channel sensors [22-24]. The two individual OCT images from the unique PS detector unit can be shown separately or combined in a total intensity image.

In this system, we integrated a gradient index (GRIN) lens into the sample arm to attain a forward view of the endoscope, as depicted in the bottom right of Figure 1. We specifically selected a GRIN lens with a diameter of 1.3 mm, closely resembling the dimensions of a typical

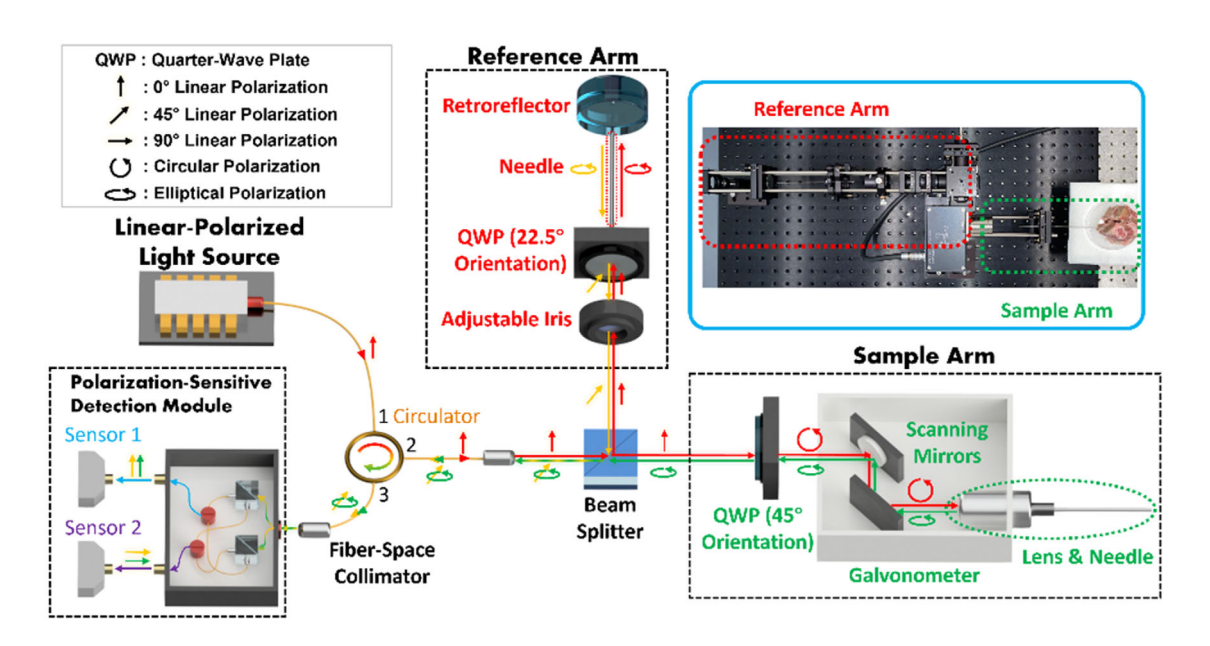


FIGURE 1 Experimental setup of the PS-OCT probe.

epidural needle. The GRIN lens measures 138.0 mm in length and offers a viewing angle of 11.0°. The proximal end of this GRIN lens is positioned near the focal plane of the scanner lens to ensure sufficient light power passes through the GRIN lens body. To counteract potential dispersion, which can affect image quality, we introduced an additional GRIN lens with identical specifications into the light path of the reference arm. This served as a compensatory element, guaranteeing precise and accurate imaging outcomes from the system. The axial imaging resolution of the PS-OCT system can reach up to 5.5 µm in air, allowing us to capture subtle structures within the samples. The scanning rate ranges from 5.5 to 76.0 kHz, and the sensitivity is 109 dB (at 5.5 kHz). The GRIN lenses are from GoFoton Corporation, and the laser and all other optical components are from Thorlabs Inc.

In addition to conventional intensity OCT imaging, PS-OCT offers supplementary tissue contrast derived from tissue birefringence characteristics. As illustrated in Figure 1, our PS-OCT endoscope incorporates two sensors designed to capture light with distinct polarization states. Here, we consider the individual intensity of sensor 1 (receiving the vertical linear polarized light) as I_1 , and the sensor 2 (receiving the horizontal linear polarized light) as I_2 . OCT intensity results are calculated with the total intensity of $I = I_1 + I_2$, where $I_1 = E_1 \times E_1^*$ and $I_2 = E_2 \times E_2^*$ (E_1^* represents the complex amplitude of the electric field). In our system, PS imaging results include phase retardation, optic axis, and degree of polarization uniformity (DOPU) [25]. Stokes parameters can be calculated as [25]:

$$Q = E_1 E_1^* - E_2 E_2^* \tag{1}$$

$$U = E_{+45^{o}} E_{+45^{o}}^{*} - E_{-45^{o}} E_{-45^{o}}^{*} = E_{1} E_{2}^{*} + E_{2} E_{1}^{*}$$
 (2)

$$V = E_R E_R^* - E_L E_L^* = i \Big(E_x E_y^* - E_y E_x^* \Big)$$
 (3)

The three PS-OCT imaging modes can be calculated following the formula below:

Phase retardation =
$$\tan^{-1} \left(\sqrt{I_1/I_2} \right) \in [0, \pi/2]$$
 (4)

Optic axis =
$$\frac{1}{2}a \tan 2(U, Q) \in [-\pi/2, \pi/2]$$
 (5)

DOPU =
$$\sqrt{\langle Q \rangle^2 + \langle U \rangle^2 + \langle V \rangle^2} \in [0,1]$$
 (6)

The incorporation of PS modes resulted in enhanced tissue contrast within the epidural samples. The assessment of phase retardation was utilized to quantitatively measure the accumulated phase change experienced by light within the tissue across the two distinct channels. Likewise, the assessment of the optic axis measured the relative angular orientation between the fast and slow axes. It is noteworthy that in instances where the sample tissue displayed a uniform birefringence property, both phase retardation and optic axis values exhibited a proportional increase with depth. Furthermore, DOPU metric facilitated a novel perspective. DOPU involved the assessment of average Stokes parameters, which in turn correlated with the extent of incident light depolarization within the sample. This comprehensive utilization of PS modes contributed to an enriched understanding of tissue properties and interactions [25].

2.2 | Deep learning procedure

Six porcine backbone samples were imaged using our PS-OCT probe. We scanned five different epidural tissue layers: (1) subcutaneous fat; (2) interspinous ligament; (3) ligamentum flavum; (4) epidural space; and (5) spinal cord, as shown in Figure 2. The image size was set at 430×950 pixels with a pixel size of 3 µm. For each backbone sample, we obtained 1000 images in each imaging mode from every tissue type, resulting in a total of 24 000 images (1000 images \times 4 imaging modes \times 6 samples). Convolutional neural network (CNN) was employed for the classification of tissue layers, enabling the automation of the epidural needle tip positioning procedure. Specifically, the ResNet50 architecture from the Keras library was utilized for this purpose [26]. The SGD optimizer was set with 50 epochs, with the learning rate of 0.01, momentum of 0.9, and decay of 0.01. The batch size was set to be 24. We employed cross-validation to optimize the number of training epochs while retaining the model architecture and all other hyperparameters consistent with our prior studies, and evaluate the prediction results [19, 27, 28]. Images were separated into six folds based on the imaging results. The dataset encompassed images from all six samples. These configurations were maintained consistently throughout all training sessions. This uniformity facilitated the comparison of performance among different imaging modes and ensured an unbiased assessment of classification capabilities. The cross-validation procedure encompassed 30 folds for each OCT imaging mode, resulting in a total of 120 folds. In addition, we conducted crosstesting with six folds. The computation time for each fold was approximately 130 min, using one NVIDIA RTX 3090 graphic card.

We used four parameters: (1) Accuracy; (2) Precision; (3) Recall; and (4) F_1 score to evaluate the prediction performance of our model. These metrics are widely used in deep learning to assess classification performance and the

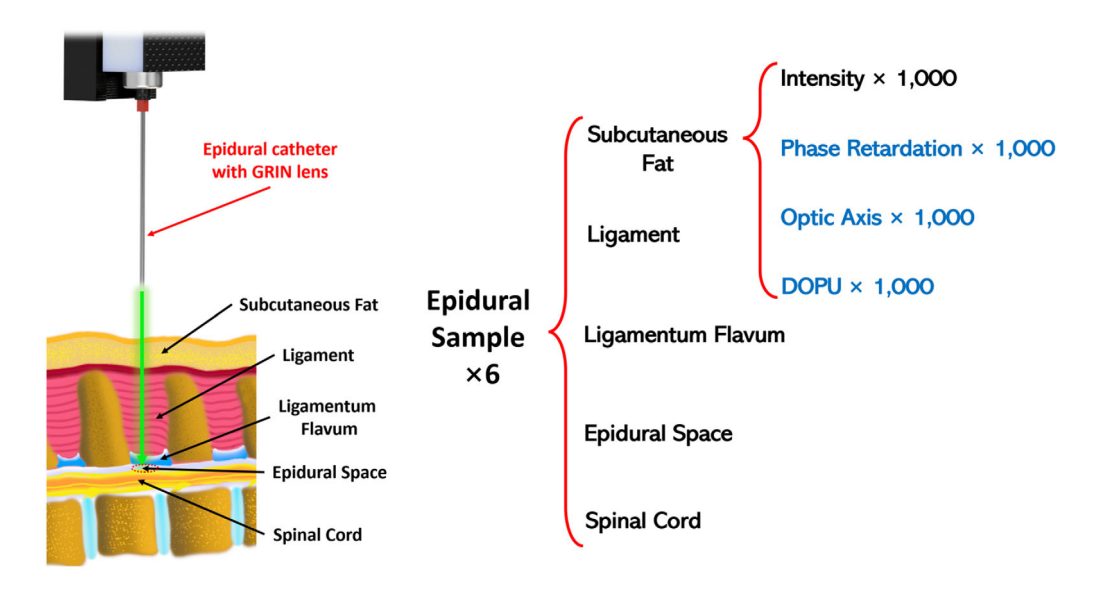
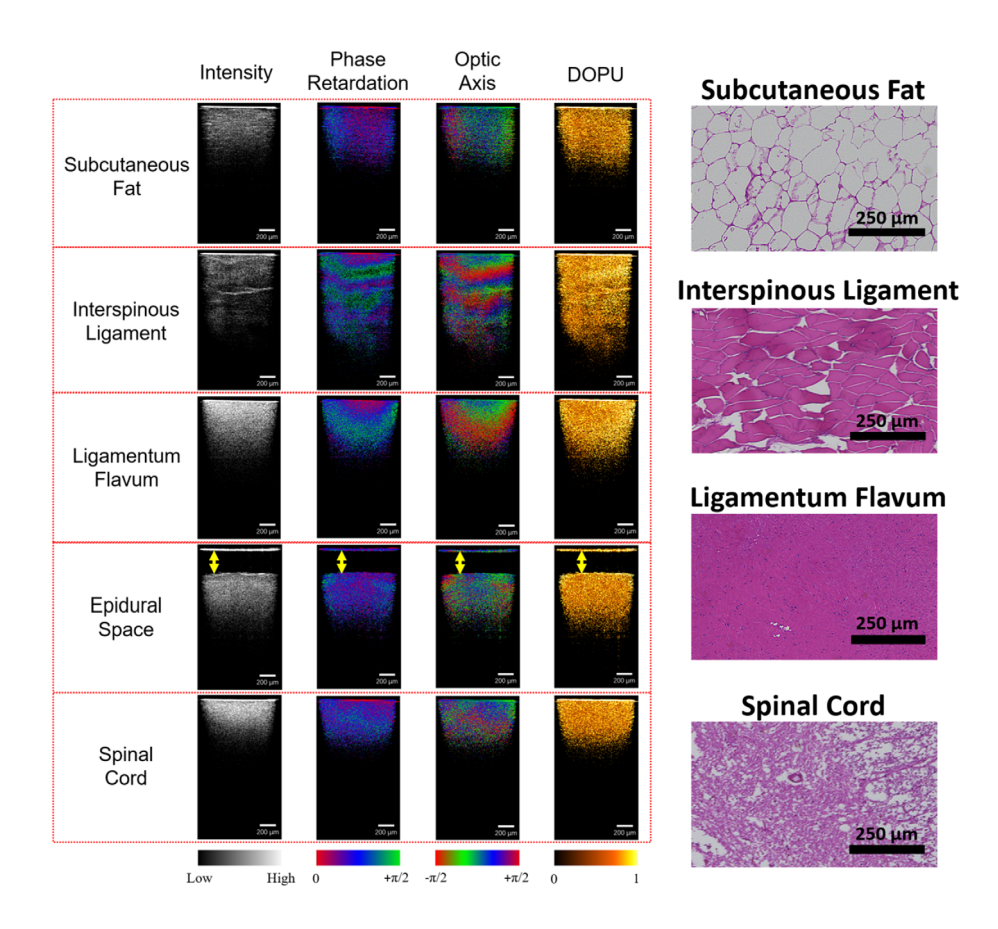


FIGURE 2 Data acquisition of the epidural tissues with the PS-OCT probe.

FIGURE 3 PS-OCT imaging results of epidural tissues and corresponding histology.



capabilities of the modes. Accuracy is the correctness of the measurements to the true value. Precision quantifies the closeness of measurements among each other. Recall indicates the proportion of relevant retrieved instances. F_1 score represents the harmonic mean between precision and recall. These metrics are computed as follows (where TP stands for true positive, FP for false positive, TN for true positive, and FN for false negative):

$$Accuracy = \frac{TP + TN}{TP + FP + TN + FN}$$
 (7)

$$Precision = \frac{TP}{TP + FP}$$
 (8)

$$Recall = \frac{TP}{TP + FN} \tag{9}$$

$$F_1 = 2 \cdot \frac{\text{Precision} \cdot \text{Recall}}{\text{Precision} + \text{Recall}} = \frac{\text{TP}}{\text{TP} + \frac{1}{2}(\text{FP} + \text{FN})}$$
 (10)

3 | RESULTS

3.1 | PS-OCT imaging results

PS-OCT images of the five epidural tissues in the four OCT modes and corresponding histology are shown in Figure 3. Regarding the OCT intensity outcomes, the five tissues exhibited distinct patterns in the OCT imaging results, which align with findings from our prior studies [9, 19]. Upon reaching the epidural space with the needle, a noticeable gap became evident between a prominent line (indicated by yellow double arrows in Figure 3) that aligned with the surface of the GRIN lens and the dura mater of the spinal cord. The tissues that the needle passed through during insertion were also distinguishable. The subcutaneous fat exhibited low imaging intensity and depth, characterized by an irregular distribution of bright bars or dots representing adipocytes. In contrast, the ligament tissue displayed the greatest imaging depth among all the tissues. Additionally, the ligament displayed horizontal lines attributed to the fibrous nature, mirroring the characteristics observed in the histology results. The flavum exhibited remarkably high brightness in the OCT intensity output, a consequence of its dense elastic fibers. Notably, when the needle penetrated the spinal cord, the tissue region appeared exceedingly bright, indicative of the densely packed nerve fibers.

In the PS imaging modes depicted in Figure 3, fiberbased tissues are notably discernible, particularly in the phase retardation and optic axis modes. Clear transverse layers were evident within the interspinous ligament and ligamentum flavum tissues, albeit exhibiting varying layer thicknesses and depths. While the spinal cord also displayed transverse layer characteristics, they were not as pronounced as those observed in the ligament and flavum tissues, which consist predominantly of elastin and collagen fibers [29, 30]. Conversely, in the case of subcutaneous fat tissue, which lacks a fiber structure, there existed lengthwise polarization contrast, a phenomenon previously documented [31]. This observation suggests a promising avenue of incorporating PS contrast into intensity results, with the potential to enhance the recognition of epidural tissues.

3.2 | Prediction results by deep learning

The classification of the five epidural tissues was conducted using the ResNet50 architecture based on its

strong performance demonstrated in our prior studies [19]. For this research, a total of 1000 cross-sectional images were captured from each tissue layer within every mode. In total, six backbone samples were utilized. Here we evaluated the classification of the five epidural groups in the four modes, respectively. The aggregated accuracy for both cross-validation and cross-testing outcomes is shown in Table 1. Notably, the intensity mode exhibited weaker predictive performance than the other PS modes. Collectively, DOPU was the most effective among the three PS modes. In comparison to the OCT intensity mode, which achieved an accuracy of 81.60%, all three PS-OCT modes exhibited superior average predictive capabilities. Specifically, phase retardation attained an accuracy of 87.39%, the optic axis yielded 85.97%, and DOPU outperformed with the highest result of 91.61%. Cross-testing accuracy was subsequently computed for each of the six testing folds. Like the cross-validation findings, DOPU exhibited the highest accuracy at 91.53%, while the OCT intensity mode recorded the lowest accuracy of 81.89%. Interestingly, in contrast to the crossvalidation outcomes, the optic axis mode surpassed the performance of the phase retardation mode. Considerable variability in testing accuracy was observed across different subjects, particularly pronounced in the case of subject 1. Subject 1 displayed the lowest performance across all four modes. This variability could be attributed to differences in tissue characteristics among various backbone samples. Furthermore, the subjects achieving the highest performance varied across different modes in the testing results. Specifically, subject 4 provided the best performance in the intensity and phase retardation modes, whereas subject 5 generated the optimal results in the optic axis and DOPU modes. This variability in performance across different imaging modes suggests a potential complementary effect that can be harnessed.

Grad-CAM heatmaps were utilized to visually show the explanations of the ResNet50 model classification as shown in Figure 4. A conspicuous disparity between the PS modes and the intensity mode lay in their distinct focal areas. In the case of the intensity mode, the model predominantly emphasized the luminous surface of the needle itself. In the three PS modes, the model exhibited a discernible shift in focus, prioritizing the tissues situated beneath the epidural space. An advantage of PS modes is that the cumulative change increases in the phase retardation and optic axis as the depth increases. The value for DOPU is not affected by depth change since it measures the Stokes parameters' average level around each pixel, whereas in OCT intensity mode, the signal decreases as the depth increases due to light scattering. In other words, the signal from

TABLE 1 Accuracies for cross-validation and cross-testing results in different imaging modes.

Dataset	Intensity	Retardation	Optic axis	DOPU				
Cross-validation								
E1	84.72%	92.00%	90.80%	94.01%				
E2	82.48%	84.21%	84.93%	91.18%				
E3	84.62%	87.78%	82.14%	91.74%				
E4	75.42%	85.95%	85.70%	92.61%				
E5	80.17%	84.74%	84.11%	89.34%				
E6	82.22%	89.64%	88.13%	90.80%				
Average	$81.60 \pm 3.47\%$	$87.39 \pm 3.02\%$	$85.97 \pm 3.07\%$	$91.61 \pm 1.60\%$				
Cross-testing								
E1	66.34%	58.16%	76.84%	75.86%				
E2	81.70%	81.82%	84.46%	87.48%				
E3	73.06%	89.48%	91.42%	90.88%				
E4	94.16%	99.54%	92.56%	98.52%				
E5	93.58%	96.66%	93.94%	97.28%				
E6	82.52%	90.38%	86.06%	99.18%				
Average	$81.89 \pm 11.02\%$	$86.01 \pm 14.97\%$	87.55 ± 6.44%	$91.53 \pm 8.98\%$				

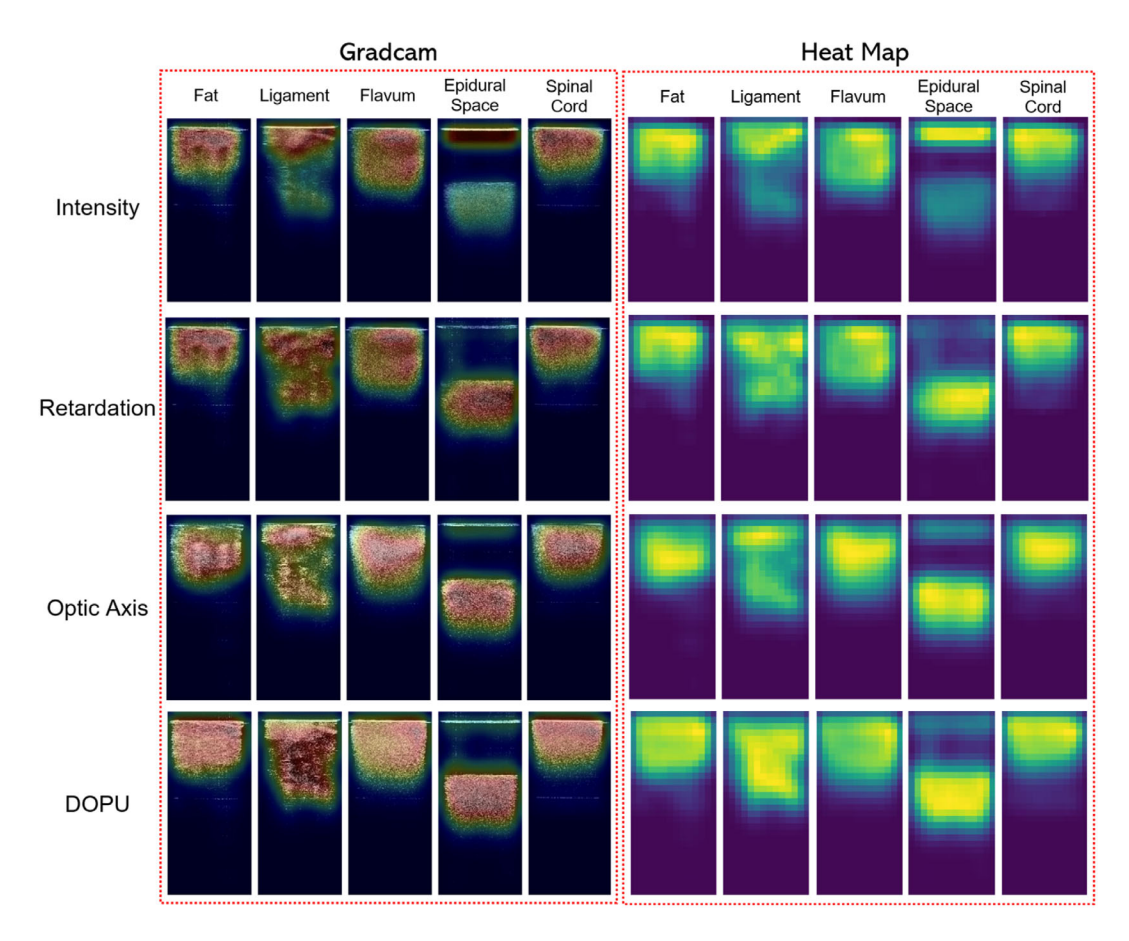


FIGURE 4 Grad-CAM and heatmap examples of different imaging results in four modes.

the deep region provides less useful information in the OCT intensity mode while less affected in the PS modes. This is clearly shown in the heatmap for

ligaments, which only covered the shallower part of the intensity image but spanned all the depth in the PS modes.

TABLE 2 Precision, recall, and F₁ score of different tissue types in each model.

OCT Imaging mode	Fat	Ligament	Flavum	Epidural space	Spinal cord
Precision					
Intensity	$81.91 \pm 1.28\%$	$86.20 \pm 4.92\%$	$76.44 \pm 5.91\%$	$99.89 \pm 2.52\%$	$79.97 \pm 4.72\%$
Retardation	$86.73 \pm 3.76\%$	$91.31 \pm 3.81\%$	$87.19 \pm 3.13\%$	$99.97 \pm 2.31\%$	$84.13 \pm 3.58\%$
Optic axis	$87.59 \pm 3.86\%$	$90.36 \pm 3.71\%$	$84.13 \pm 3.87\%$	$97.72 \pm 1.96\%$	$83.02 \pm 2.33\%$
DOPU	$94.80 \pm 2.76\%$	$96.03 \pm 4.01\%$	$87.11 \pm 3.32\%$	$99.69 \pm 0.32\%$	$88.94 \pm 1.65\%$
Recall					
Intensity	$92.85 \pm 3.05\%$	$82.17 \pm 2.54\%$	$64.10 \pm 3.77\%$	$94.38 \pm 0.11\%$	$74.52 \pm 2.81\%$
Retardation	$83.78 \pm 3.52\%$	$86.63 \pm 2.25\%$	$82.94 \pm 2.57\%$	$95.35 \pm 0.02\%$	$88.26 \pm 2.82\%$
Optic Axis	$83.50 \pm 1.66\%$	$87.20 \pm 2.31\%$	$74.41 \pm 2.90\%$	$94.73 \pm 1.15\%$	$90.00 \pm 2.74\%$
DOPU	$88.73 \pm 0.98\%$	$86.27 \pm 0.75\%$	$88.57 \pm 3.56\%$	$99.46 \pm 0.31\%$	$95.03 \pm 2.91\%$
F1					
Intensity	$85.82 \pm 1.93\%$	$80.17 \pm 3.96\%$	$64.07 \pm 4.37\%$	$96.47 \pm 1.66\%$	$73.38 \pm 3.44\%$
Retardation	$82.90 \pm 3.39\%$	$87.65 \pm 3.17\%$	$84.13 \pm 2.54\%$	$97.07 \pm 1.56\%$	$83.97 \pm 3.28\%$
Optic Axis	$83.88 \pm 2.60\%$	$86.40 \pm 2.57\%$	$76.13 \pm 2.79\%$	$95.71 \pm 1.31\%$	$84.74 \pm 1.72\%$
DOPU	$90.85 \pm 1.87\%$	$89.22 \pm 3.00\%$	$86.87 \pm 3.22\%$	$99.56 \pm 0.23\%$	$90.70 \pm 1.87\%$

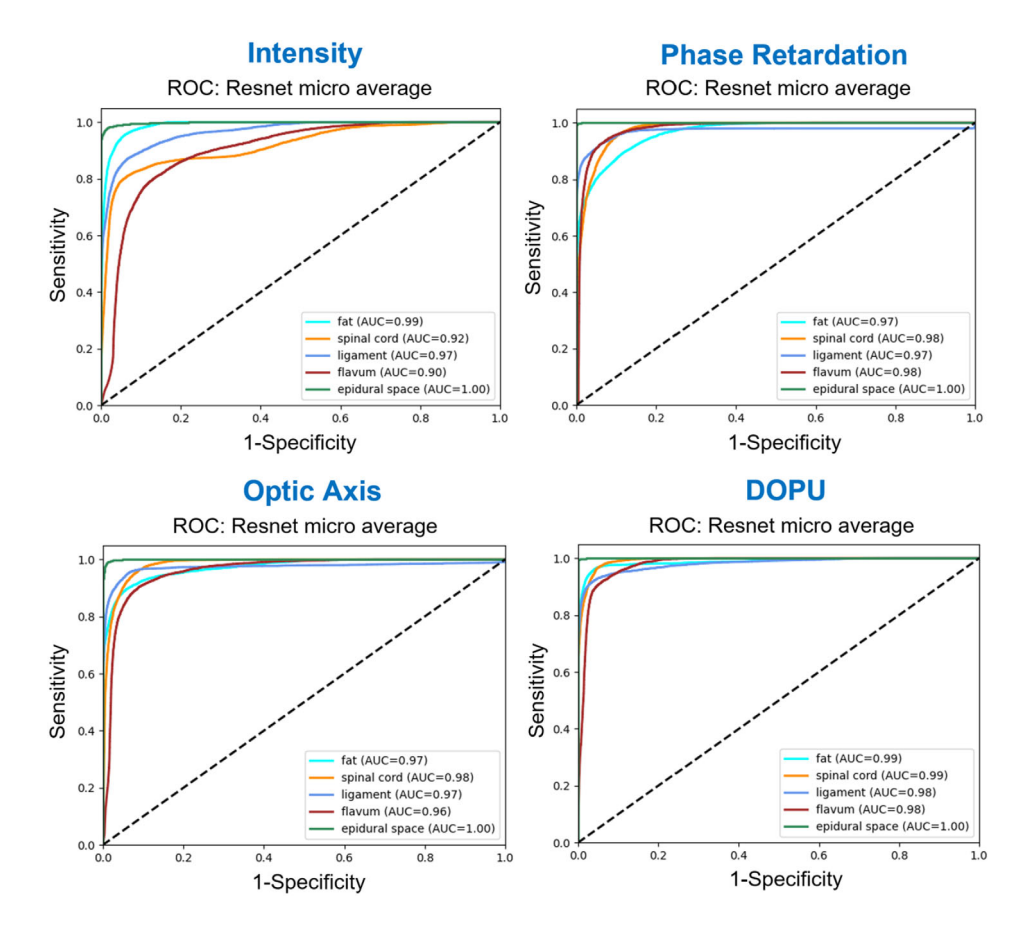


FIGURE 5 ROC curves of different imaging modes. AUC, Area under the ROC curve, ROC, receiver operating characteristic.

Table 2 displays the classification outcomes for various tissue types, whereas the associated receiver operating characteristic curves are illustrated in Figure 5. From the averaged values for each tissue layer, epidural

space was the most easily recognizable due to the gap between the needle tip and the tissue surface and DOPU presented the best F_1 score of 99.56%. Given that the epidural space is the target destination for the epidural

needle, accurate identification of this site ensures precise needle placement. Compared with other tissues, flavum is the most difficult to identify but the results in retardation and DOPU are significantly improved (>84% F1 Score) compared with 64% F1 Score from intensity mode. Fat, ligament, and spinal cord all had over 80% results in all the values (precision, recall, and F1 Score) in the PS modes. Overall, DOPU mode provided the best measurements among all the OCT imaging modes. Retardation and Optic Axis also gave better performances than intensity. Therefore, in comparison with conventional structural OCT imaging, PS-OCT imaging can provide better classification performance using more tissue information.

4 | DISCUSSION

In this study, we assessed the performance of a forwardview PS-OCT probe for guiding epidural anesthesia needle placement. Our innovative system offers significantly improved resolution compared to conventional imaging techniques such as ultrasound and fluoroscopy, providing a clearer front view of the epidural needle. By employing PS-OCT, our system can acquire both intensity and PS signals and achieve a superior axial resolution of 5.5 μm, outperforming our previous research on SS-OCT with an axial resolution of \sim 14.0 µm. The high-resolution imaging results offered intricate details, allowing medical professionals to discern the epidural tissue type and accurately determine the needle tip location, which explained the significant increase in cross-validation accuracy from 66% using SS-OCT to 81.60% using intensity mode alone. Furthermore, the imaging results obtained in PS modes revealed distinct features of the five epidural tissue layers, enabling more effective differentiation between them compared to the intensity mode alone. This enhanced understanding of tissue characteristics could aid in optimizing the needle guidance procedure for epidural anesthesia.

Besides the intensity and penetration depth contrast in the intensity OCT mode, PS modes enhanced the feature of the tissues with fiber structures such as ligament, flavum, and spinal cord. We conducted a thorough assessment of our models' generalization performance using a nested cross-validation and cross-testing procedure. This allowed us to gain valuable insights into their robustness and potential for clinical applications. The cross-testing results showed an excellent average accuracy of 91.53% in DOPU mode, with phase retardation and optic axis also yielding accuracies at 86.01% and 87.55%, respectively. In contrast, intensity modes only exhibited a prediction accuracy of 81.89% even with the

improved imaging resolution. Further evaluation using precision, recall, and F1 scores for each tissue type revealed that the epidural space was consistently the easiest tissue layer to recognize in both PS modes and intensity modes. This finding is particularly promising as the epidural needle needs to be placed inside the epidural space, making its recognition a critical step. The recognition accuracies were also improved for the other tissues in all the three PS modes. In general, the three PS modes provided better predictions than intensity except for fat, and DOPU yielded the highest F₁ score across all five epidural tissue types. Importantly, the diverse imaging modes demonstrated unique capabilities in identifying specific tissues. By integrating the strengths of each mode, we anticipate significant improvements in tissue classification accuracy. The inference time on NVIDIA RTX 3090 GPUs was 0.0314 s per image and 0.1256 s for all the four imaging modes on average, thus real-time prediction using all four modes can still be achieved in our system. When multiple GPUs are available, the inference time can be further reduced by parallelizing the inferencing across GPUs.

The endoscopic PS-OCT system developed in this study was based on a single input polarization state, thus the polarization parameters (phase retardation, optic axis, and DOPU) were all cumulative values [32]. The cumulative phase retardation only indicated the phase retardation between the principal polarization states along the complete optical path through the tissue rather than the phase retardation effect at a single depth location [33, 34]. Therefore, the 'local' polarization information was not able to be quantitatively provided. On the other hand, due to the direct proportionality between the local birefringence mode and the actual birefringent signal per pixel in the OCT images, the local polarization signal suffers from diminished sensitivity [35, 36]. Compared with the local polarization mode, the cumulative polarization mode exhibited higher sensitivity and demanded a considerably simplified system, so it remained the preferred choice for image classification purposes [33, 35, 37]. Considering the key to the epidural guidance application is the differentiation between different spinal tissues, cumulative polarization parameters were applied in this study. Additionally, we plan to upgrade our system to enhance its usability and convenience in clinical settings. To validate the clinical translatability of our PS-OCT probe, we will continue to improve our technology using in-vivo pig models. Furthermore, considering the anatomical variations and tissue properties differences between pig and human epidural tissues, we will continue this project on human samples in the future. To improve the automatic tissue prediction in our future work, we will combine PS-OCT and intensity OCT as an integrated

input into a multichannel CNN [38] or an ensemble learning system [39]. By leveraging the strengths of individual modes for identifying specific tissues, this integrated approach is expected to achieve an enhanced overall tissue recognition accuracy, albeit with the tradeoff of increased computational costs and model complexity. Furthermore, by employing various model interpretation methods [40, 41], we can gain insights into which imaging features and modalities contribute most to accurate classifications of different tissues. This will help us further optimize our OCT imaging technique and enhance its diagnostic capabilities. By pursuing these steps, we aim to advance the capabilities of our PS-OCT probe and deep learning model, ultimately contributing to improved epidural anesthesia needle guidance procedures and enhancing clinical outcomes.

ACKNOWLEDGMENTS

This work was supported by grants from the Institutional Research Grant number IRG-19-142-01 from American Cancer Society, National Science Foundation (OIA-2132161, 2238648), National Institute of Health (R01DK133717, P20GM135009, P20GM103639, P30CA225520, NIGMSU54GM104938), Oklahoma Center for the Advancement of Science and Technology (HR23-071), and the medical imaging COBRE (P20GM135009). Histology service provided by the Tissue Pathology Shared Resource was supported in part by the and the National Institutes of Health. The content is solely the responsibility of the authors and does not necessarily represent the official views of the National Institutes of Health or the Indian Health Service. Financial support was provided by the OU Libraries' Open Access Fund.

CONFLICT OF INTEREST STATEMENT

The authors declare no conflicts of interest.

DATA AVAILABILITY STATEMENT

The data that support the findings of this study are openly available in Endoscopic_OCT_Epidural at https://github.com/thepanlab/Endoscopic_OCT_Epidural.git.

ORCID

Chen Wang https://orcid.org/0000-0003-4645-3227

REFERENCES

- [1] V. Svircevic, D. van Dijk, A. P. Nierich, M. P. Passier, C. J. Kalkman, G. J. M. G. van der Heijden, L. Bax, *Anesthesiology* 2011, 114, 271.
- [2] H. Hayashi, T. Ochiai, H. Shimada, Y. Gunji, Surg. Endosc. Other Interv. Tech. 2005, 19, 1172.

- [3] R. J. Moraca, D. G. Sheldon, R. C. Thirlby, Ann. Surg. 2003, 238, 663.
- [4] A. N. A. Hernandez, P. Singh, *StatPearls [Internet]*, StatPearls Publishing, Treasure Island, **2022**.
- [5] R. Patel, I. Urits, V. Orhurhu, M. S. Orhurhu, J. Peck, E. Ohuabunwa, A. Sikorski, A. Mehrabani, L. Manchikanti, A. D. Kaye, R. J. Kaye, J. A. Helmstetter, O. Viswanath, *Curr. Pain Headache Rep.* 2020, 24, 1.
- [6] B. Chekol, T. Yetneberk, D. Teshome, Ann. Med. Surg. 2021, 66, 102456.
- [7] M. Tripathi, S. S. Nath, R. K. Gupta, Anesth. Analg. 2005, 101, 1209 table of contents.
- [8] M. J. Frumin, H. Schwartz, J. J. Burns, B. B. Brodie, E. M. Papper, Anesthesiology 1953, 14, 576.
- [9] Q. Tang, C. P. Liang, K. Wu, A. Sandler, Y. Chen, Quant. Imaging Med. Surg. 2015, 5, 118.
- [10] S. Y. Kang, O. N. Kashlan, R. Singh, R. Rane, N. M. Adsul, S. C. Jung, J. Yi, H. S. Cho, H. S. Kim, I. T. Jang, S. H. Oh, J. Pain Res. 2020, 13, 211.
- [11] H. Elsharkawy, W. Saasouh, R. Babazade, L. M. Soliman, J. L. Horn, S. Zaky, *Pain Med.* 2019, 20, 1750.
- [12] M. Yeager, E. E. Bae, M. C. Parra, P. A. Barr, A. K. Bonham, B. D. Sites, Acta Anaesthesiol. Scand. 2016, 60, 513.
- [13] S. Y. Kang, H. S. Cho, J. Yi, H. S. Kim, I. T. Jang, D. H. Kim, World Neurosurg. 2022, 159, e103.
- [14] J. Richardson, G. J. Groen, Contin. Educ. Anaesth. Crit. Care Pain 2005, 5, 98.
- [15] S. D. Waldman, Pain management E-book, Elsevier Health Sciences, Philadelphia, PA, 2011.
- [16] S. P. Lin, M. S. Mandell, Y. Chang, P. T. Chen, M. Y. Tsou, K. H. Chan, C. K. Ting, Br. J. Anaesth. 2012, 108, 302.
- [17] T. A. Anderson, J. W. Kang, T. Gubin, R. R. Dasari, P. T. C. So, Anesthesiology 2016, 125, 793.
- [18] D. Huang, E. A. Swanson, C. P. Lin, J. S. Schuman, W. G. Stinson, W. Chang, M. R. Hee, T. Flotte, K. Gregory, C. A. Puliafito, J. G. Fujimoto, *Science* 1991, 254, 1178.
- [19] C. Wang, P. Calle, J. C. Reynolds, S. Ton, F. Yan, A. M. Donaldson, A. D. Ladymon, P. R. Roberts, A. J. de Armendi, K. M. Fung, S. S. Shettar, C. Pan, Q. Tang, Sci. Rep. 2022, 12, 9057.
- [20] C. Wang, P. Calle, J. C. Reynolds, N. B. Ton, F. Yan, A. M. Donaldson, A. D. Ladymon, P. R. Roberts, A. J. De Armendi, K. M. Fung, S. S. Shettar, Endoscopic Optical Coherence Tomography for Epidural Anesthesia Guidance (Conference Presentation), Vol. PC11949, SPIE BiOS, San Francisco, CA, 2022.
- [21] M. R. Hee, E. A. Swanson, J. G. Fujimoto, D. Huang, *JOSA B* 1992, 9, 903.
- [22] J. F. de Boer, T. E. Milner, M. J. C. van Gemert, J. S. Nelson, Opt. Lett. 1997, 22, 934.
- [23] C. K. Hitzenberger, E. Götzinger, M. Sticker, M. Pircher, A. F. Fercher, Opt. Express 2001, 9, 780.
- [24] J. E. Roth, J. A. Kozak, S. Yazdanfar, A. M. Rollins, J. A. Izatt, *Opt. Lett.* **2001**, *26*, 1069.
- [25] J. F. de Boer, C. K. Hitzenberger, Y. Yasuno, Biomed. Opt. Express 2017, 8, 1838.
- [26] K. He, X. Zhang, S. Ren, J. Sun, Deep residual learning for image recognition. In Proceedings of the IEEE Conference on Computer Vision and Pattern Recognition. 2016.

- [27] C. Wang, J. C. Reynolds, P. Calle, A. D. Ladymon, F. Yan, Y. Yan, S. Ton, K. M. Fung, S. G. Patel, Z. Yu, C. Pan, Q. Tang, J. Biophotonics 2022, 15, e202100347.
- [28] C. Wang, P. Calle, N. B. Tran Ton, Z. Zhang, F. Yan, A. M. Donaldson, N. A. Bradley, Z. Yu, K. M. Fung, C. Pan, Q. Tang, Biomed. Opt. Express 2021, 12, 2404.
- [29] S. Hirabayashi, Spine Surg Relat Res 2017, 1, 158.
- [30] J. Iwanaga, E. Simonds, E. Yilmaz, M. Schumacher, M. Patel, R. S. Tubbs, Asian. J. Neurosurg. 2019, 14, 1203.
- [31] Z. Ding, Q. Tang, C. P. Liang, K. Wu, A. Sandlerc, H. Li, Y. Chen, *IEEE Photonics J.* **2016**, *8*, 1.
- [32] Z. Ding, C.-P. Liang, Y. Chen, Front. Optoelectron. 2015, 8, 128.
- [33] M. G. Gräfe, J. A. van de Kreeke, J. Willemse, B. Braaf, Y. de Jong, H. S. Tan, F. D. Verbraak, J. F. de Boer, *Transl. Vis. Sci. Technol.* 2020, 9, 13.
- [34] B. Braaf, K. A. Vermeer, M. de Groot, K. V. Vienola, J. F. de Boer, Biomed. Opt. Express 2014, 5, 2736.
- [35] F. Feroldi, J. Willemse, V. Davidoiu, M. G. O. Gräfe, D. J. van Iperen, A. W. M. Goorsenberg, J. T. Annema, J. M. A. Daniels, P. I. Bonta, J. F. de Boer, *Biomed. Opt. Express* 2019, 10, 3070.

- [36] M. Villiger, D. Lorenser, R. A. McLaughlin, B. C. Quirk, R. W. Kirk, B. E. Bouma, D. D. Sampson, Sci. Rep. 2016, 6, 6.
- [37] J. Willemse, M. G. O. Gräfe, J. A. van de Kreeke, F. Feroldi, F. D. Verbraak, J. F. de Boer, Opt. Lett. 2019, 44, 3893.
- [38] M. Y. Zhao, C. H. Chang, W. Xie, Z. Xie, J. Hu, *IEEE Access* 2020, 8, 44111.
- [39] A. Kumar, J. Kim, D. Lyndon, M. Fulham, D. Feng, IEEE J. Biomed. Health Inform. 2017, 21, 31.
- [40] A. Badre, C. L. Pan, IEEE Access 2022, 10, 36166.
- [41] A. Badre, C. L. Pan, PLoS Comput. Biol. 2023, 19, e1011211.

How to cite this article: C. Wang, Y. Liu, P. Calle, X. Li, R. Liu, Q. Zhang, F. Yan, K. Fung, A. K. Conner, S. Chen, C. Pan, Q. Tang, *J. Biophotonics* **2023**, e202300330. https://doi.org/10.1002/jbio.202300330